

Forced and Free Intraseasonal Variability over the South Asian Monsoon Region Simulated by 10 AGCMs

MAN LI C. WU AND SIEGFRIED SCHUBERT

Data Assimilation Office, NASA Goddard Space Flight Center, Greenbelt, Maryland

IN-SIK KANG

School of Earth and Environmental Sciences, Seoul National University, Seoul, South Korea

DUANE WALISER

Institute for Terrestrial and Planetary Atmospheres, State University of New York at Stony Brook, Stony Brook, New York

(Manuscript received 1 December 2001, in final form 20 May 2002)

ABSTRACT

This study examines intraseasonal (20–70 day) variability in the South Asian monsoon region during 1997/98 in ensembles of 10 simulations with 10 different atmospheric general circulation models. The 10 ensemble members for each model are forced with the same observed weekly sea surface temperature (SST) but differ from each other in that they are started from different initial atmospheric conditions.

The results show considerable differences between the models in the simulated 20–70-day variability, ranging from much weaker to much stronger than the observed. A key result is that the models do produce, to varying degrees, a response to the imposed weekly SST. The forced variability tends to be largest in the Indian and western Pacific Oceans where, for some models, it accounts for more than a quarter of the 20–70-day intraseasonal variability in the upper-level velocity potential during these two years.

A case study of a strong observed Madden–Julian oscillation (MJO) event shows that the models produce an ensemble mean eastward-propagating signal in the tropical precipitation field over the Indian Ocean and western Pacific, similar to that found in the observations. The associated forced 200-mb velocity potential anomalies are strongly phase locked with the precipitation anomalies, propagating slowly to the east (about 5 m s^{-1}) with a local zonal wavenumber-2 pattern that is generally consistent with the developing observed MJO. The simulated and observed events are, however, approximately in quadrature, with the simulated response leading by 5–10 days. The phase lag occurs because, in the observations, the positive SST anomalies develop upstream of the main convective center in the subsidence region of the MJO, while in the simulations, the forced component is in phase with the SST.

For all the models examined here, the intraseasonal variability is dominated by the free (intraensemble) component. The results of the case study presented here show that the free variability has a predominately zonal wavenumber-1 pattern, and has propagation speeds ($10\text{--}15 \text{ m s}^{-1}$) that are more typical of observed MJO behavior away from the convectively active regions. The free variability appears to be synchronized with the forced response, at least during the strong event examined here.

The results of this study support the idea that coupling with SSTs plays an important, though probably not dominant, role in the MJO. The magnitude of the atmospheric response to the SST appears to be in the range of 15%–30% of the 20–70-day variability over much of the tropical eastern Indian and western Pacific Oceans. The results also highlight the need to use caution when interpreting atmospheric model simulations in which the prescribed SST resolves MJO timescales.

1. Introduction

It is now well established that latent heat flux anomalies associated with the Madden–Julian oscillation (MJO; Madden and Julian 1972) play an important role in the development of intraseasonal sea surface tem-

perature (SST) anomalies in the Indian and western Pacific Oceans (Krishnamurti et al. 1988; Zhang and McPhaden 1995). Recent studies (e.g., Zhang 1996; Hendon and Glick 1997; Lau and Sui 1997; Sperber et al. 1997; Shinoda et al. 1998; Jones et al. 1998) suggest that both MJO-induced surface evaporative and radiative flux anomalies contribute to intraseasonal anomalies in SST. Hendon and Glick (1997) show that there are differences between the ocean basins, in that the Indian Ocean SST anomalies are primarily driven by surface

Corresponding author address: Man Li C. Wu, Data Assimilation Office, NASA Goddard Space Flight Center, Greenbelt, MD 20771.
E-mail: mwu@dao.gsfc.nasa.gov

insolation anomalies associated with convection, while the western Pacific SST anomalies are driven by both surface evaporation and insolation anomalies. Jones et al. (1998) provide a general picture of the MJO–SST relationship in which clear skies and reduced surface winds ahead of the convection anomaly result in an increase in surface net shortwave radiation and decreased surface latent heat fluxes that favor positive SST anomalies. As the convection moves eastward over the warmer SST, the increased cloudiness and enhanced surface westerlies lead to reduced surface shortwave radiation and enhanced surface evaporation that favor negative SST anomalies.

Wang and Xie (1998) used a simplified linear coupled ocean–atmospheric model to carry out a theoretical analysis of the impact of SST feedback on the MJO. They found that the coupling produces SST anomalies that lead the convective anomalies and act to destabilize the atmospheric moist Kelvin wave and reduce its phase speed to observed values. Flatau et al. (1997) investigated the impact of SST on the simulated MJO in an aquaplanet atmospheric general circulation model (AGCM) with a simple empirical representation of an ocean mixed layer. They found that the coupled model produced a stronger and slower MJO. They suggest that this occurred as a result of warmer SSTs to the east of the convection that acted to destabilize the atmosphere by increasing the moist static energy. Waliser et al. (1999) show that, in another AGCM coupled to a slab ocean model, an improved simulation of the MJO occurs compared with simulations with the same model that used a prescribed SST. They also attributed the improvements in the simulations to feedbacks with the SSTs. They show, however, that positive SST anomalies forced by latent heating and, to a lesser extent, insolation anomalies to the east of the convection act to reinforce meridional convergence associated with the wave conditional instability of the second kind (CISK) mechanism operating in the AGCM. Hendon (2000) investigated the impact of air–sea coupling associated with the MJO in yet another AGCM coupled to a comprehensive ocean mixed layer model. That study found little impact of the coupling on the simulated MJO and showed that this was primarily due to deficiencies in the AGCM’s latent heat flux that did not allow the formation of coherent SST anomalies.

Recently, Schubert and Wu (2001) found that, in an ensemble of AGCM runs with prescribed *weekly* SSTs, a significant forced “MJO-like” response occurred in the simulations during those times when strong MJO events occurred in the observations. This was interpreted as evidence of a potentially important feedback of the intraseasonal SST variations on the MJO. The current study extends the Schubert and Wu analysis by carrying out a more detailed analysis of the response to SST in ensembles of simulations with 10 different AGCMs. The model runs were carried out as part of the Asian–Australian Monsoon AGCM intercomparison

project sponsored by the World Climate Research Program (WCRP) Climate Variability and Predictability (CLIVAR) Asian–Australian Monsoon panel (Kang et al. 2002).

Section 2 describes the simulated and observed data and outlines the diagnostics and processing steps used in the analysis. The results are presented in section 3. In section 3a we present a review of the basic structure of the MJO and its links to SST based on 17 years of the National Centers for Environmental Prediction–National Center for Atmospheric Research (NCEP–NCAR) reanalysis and the Global Precipitation Climatology Project (GPCP) precipitation observations. Section 3b describes the simulated and the observed intraseasonal variability for 1997/98. This includes the partition of the simulated variance into a forced and free component. Section 3c examines the link between SST and the MJO for a particularly strong observed MJO event. The discussion and conclusions are given in section 4.

2. Data and analysis methods

a. Model simulations

The focus of the analysis is on the 2-yr 10-member ensemble simulations from 10 different AGCMs made available through the CLIVAR/GCM Monsoon intercomparison project. The AGCM simulations used here are from the following institutions: Center for Ocean–Land–Atmosphere Studies (COLA); Department of Numerical Mathematics, Russian Academy of Sciences (DNM); Goddard Space Flight Center (GSFC) Earth Observing System (GEOS); State University of New York–Goddard Laboratory for Atmospheres (SUNY–GLA); Geophysical Fluid Dynamics Laboratory (GFDL); Institute of Atmospheric Physics (IAP, China); Indian Institute of Technology, Madras (IITM, Chennai, India); Meteorological Research Institute (MRI, Japan); National Center for Atmospheric Research (NCAR); and Seoul National University (SNU, Seoul, Korea). The details of the intercomparison project and the description of the participated models can be found in Kang et al. (2002).

The 10-member ensemble AGCM simulations were performed for the period 1 September 1996–31 August 1998. This period was originally chosen because it offered the chance to look in detail at how the models simulated the impacts on the Asian monsoon of a major El Niño–Southern Oscillation (ENSO) event. The 10 ensemble members differ only in the initial atmospheric conditions. The SSTs are prescribed from the weekly SST data of Reynolds and Smith (1994). In addition to the 1997/98 ensembles, the models were run for the period 1979–98 with prescribed observed monthly SSTs (see Kang et al. 2002). These longer runs were used to produce, for each model, a 5-day-average (pentad) climatology that serves as a reference for analyzing the 1997/98 time period. The basic model variables used

here are precipitation and the 200- and 850-mb winds. All GCM data were converted to a common spatial resolution of 2.0° latitude \times 2.5° longitude, although the spatial resolution of the models varies from rhomboidal truncation at wavenumber 15 to triangular truncation at wavenumber 42. The velocity potential and streamfunction fields were computed from the winds at the common resolution.

b. Observed data

The atmospheric circulation and surface fluxes are obtained from the NCEP–NCAR reanalysis (Kalnay et al. 1996). In section 3a, we analyze a long record (1982–99) of NCEP–NCAR winds and surface latent heat and net shortwave fluxes to review the link between the MJO and sea surface temperatures. In sections 3b and 3c, we use the 1997/98 NCEP–NCAR 850- and 200-mb winds to compare with the model simulations for that time period. The precipitation data consist of two GPCP products with submonthly temporal resolution. The first is a daily, 1° horizontal resolution, multisatellite precipitation dataset available beginning in January 1997 (Huffman et al. 2001). The second is a 5-day-averaged (pentad) precipitation dataset available beginning in January 1979 (Xie and Arkin 1997), and used here for the period 1982–98. The pentad data were produced by merging several kinds of precipitation data, including gauge observations and estimates inferred from infrared radiation (IR), outgoing longwave radiation (OLR), microwave sounding unit (MSU), and Special Sensor Microwave Imager (SSM/I) satellite observations.

c. Data processing

We took several steps to isolate the intraseasonal variability in both the models and the observations. For the reanalysis, pentad anomalies are computed from the 1982–98 pentad climatology. For the simulations, pentad anomalies were computed from each model's pentad climatology described earlier. Unless noted otherwise, all anomalies are filtered to retain only the timescales between 20 and 70 days. The filter is a symmetric, 4-pole, low-pass, tangent Butterworth filter described in Oppenheim and Schaffer (1975). The filter is applied twice, first retaining timescales longer than 20 days and then retaining timescales longer than 70 days. The band-pass data are obtained by subtracting the two filtered datasets. In our calculations, the end-point effect is reduced by extending the ends of the series by duplicating the beginning and ending values.

1) FORCED AND FREE VARIABILITY

For the simulations, the total variance of a quantity (x) is divided into forced (interensemble) and free (intraensemble) components. This terminology is consistent with the idea that the ensemble mean of each model

must be forced by the specified boundary conditions (SST anomalies), while the variations about each model's ensemble mean is uncorrelated with the SST, and therefore must be internally generated. As we shall see, the latter are not strictly free oscillations in that the intraensemble variability may be synchronized in time by the SST. An unbiased estimate of the interensemble variance for a particular model is (see, e.g., Rowell et al. 1995)

$$s_\beta^2 = \frac{n}{n-1}[(\bar{x} - [\bar{x}])^2] - \frac{1}{m}s_\varepsilon^2. \quad (1)$$

Here the overbar denotes a mean over the $m = 10$ ensemble members, the square brackets denote a mean over n independent time periods, and the subscript β indicates that it is the forced variance. The second term on the right-hand side of (1) is proportional to the intraensemble or free variance (indicated by subscript ε) and ensures that the estimate of the forced variance is unbiased. An unbiased estimate of the free variance is

$$s_\varepsilon^2 = \frac{m}{m-1}[\overline{(x - \bar{x})^2}]. \quad (2)$$

The total variance is defined as the sum of (1) and (2). The ratio of the forced variance to the total variance is defined as

$$P_\beta = \frac{s_\beta^2}{s_\beta^2 + s_\varepsilon^2}. \quad (3)$$

The ratio of the forced to free variance is defined as

$$U = \frac{s_\beta^2}{s_\varepsilon^2}. \quad (4)$$

Model-average estimates of P_β and U are obtained as in (3) and (4), except that s_β^2 and s_ε^2 are replaced by the averages of all the individual model forced and free variance estimates. For the observations or reanalysis we have only one realization, so that the total variance is defined as

$$s^2 = \frac{n}{n-1}[(x - [x])^2]. \quad (5)$$

2) EOF AND COMPOSITE ANALYSIS

In section 3a, we produce a composite picture of the evolution of the MJO. The composite is produced from the 17 yr (1982–98) of NCEP–NCAR reanalysis data using the leading principal component of the filtered (20–70 day) 200-mb velocity potential field as an index of the MJO. The principal components are the expansion coefficients of a complex empirical orthogonal function (CEOFs; e.g., Pfeffer et al. 1990) decomposition. The CEOF decomposition provides an efficient spatial representation of a traveling disturbance such as the MJO. Details of the CEOF formulation may be found in Chang et al. (2001) and are not repeated here. The results of

the CEOF decomposition lead to an expansion of a time series of fields $Z(x, y, t)$ that has the form

$$Z(x, y, t) = \sum_{p=1}^N \alpha_p(t) \beta_p(x, y) \cos[\theta_p(x, y) - \phi_p(t)], \quad (6)$$

where each component of (6) may be thought of as representing a wave with phase shape $\cos[\theta_p(x, y)]$ and time-dependent phase $\phi_p(t)$, the amplitude of which is modulated in space by $\beta_p(x, y)$ and in time by $\alpha_p(t)$.

The composite fields described in the next section are obtained by averaging the fields for the appropriate phase of the first CEOF only during those times when the magnitude of $\alpha_p(t)$ exceeded one standard deviation.

3. Results

The results are divided into three sections. In section 3a we present a review of the basic structure of the MJO and its links to SST based on 17 yr of observations and analyses. Section 3b evaluates the 1997/98 observed and simulated intraseasonal variability, and section 3c is a case study of a strong MJO event during 1997.

a. The composite MJO

In this section we summarize the relevant characteristics of the canonical “observed” MJO in order to provide a context for interpreting the subsequent results that are based entirely on the period 1997/98 (the period covered by the model simulations). We begin by computing the complex EOFs [CEOFs, see section 2c(2)] of the filtered (20–70 days) 200-mb velocity potential anomalies (VLPAs) for all seasons for the period 1982–98. The leading CEOF accounts for three-fourths of the filtered variance and represents a traveling zonal wavenumber-1 disturbance. The results (Figs. 1–2) are displayed as composites, computed using the time series of the amplitude of the leading CEOF as an index and averaging according to the phase of the oscillation. Values are included in the composite only for those times when the amplitude of the CEOF exceeds one standard deviation. The zonal wavenumber-1 structure and eastward propagation of the VLPAs shown in these figures are consistent with previous analyses of the MJO (e.g., Weickmann et al. 1985; Hendon and Salby 1994). The timescale of the oscillation is (again consistent with the MJO) predominantly between 30 and 60 days (see Chang et al. 2001), so that the panels in Fig. 1 show events that are approximately 5 days apart.

The left panel of Fig. 1 shows the composite-filtered 200-mb velocity potential (contoured) and precipitation (shaded) anomalies associated with CEOF 1. The composite picture shows that, as the rising branch of the MJO enters the Indian Ocean, the precipitation is enhanced on its leading edge (phases -180° to -135°). The maximum precipitation anomaly occurs at a phase of -90° , when it is centered on the rising branch of the

MJO near 90°E longitude. This is consistent with previous studies (e.g., Hendon and Salby 1994). At a phase of -45° the precipitation anomalies split, with two local maxima (one north and one south of the equator) on the trailing edge of the rising branch, and a single maximum on the leading edge. The northern precipitation anomaly subsequently moves north-northeast over India, the Bay of Bengal, Indochina, and the Pacific warm pool. This is reminiscent of the typical evolution of low-frequency intraseasonal summer monsoon fluctuations in that region (e.g., Yasunari 1981; Wu et al. 1999). Beyond a phase of 0° , the rising branch of the MJO becomes decoupled from the precipitation anomalies that themselves become weak. As the sinking branch enters the Indian Ocean (phase $>0^\circ$), the precipitation anomalies are approximately repeated but with the opposite sign to those during the phases -180° to 0° .

The right panel of Fig. 1 is the same as the left panel except for the composite evolution of the filtered SST anomalies. The SST anomalies show evidence of eastward propagation over the Indian Ocean and western Pacific warm pool as the CEOF cycles through the phases -180° to 0° . In this region, the warmest SSTs tend to occur on the leading edge of the rising branch of the MJO. In the eastern Pacific, the SST anomalies tend to be positive during the phases -180° to -135° and negative during the phases -90° and $+90^\circ$ to $+180^\circ$. This suggests that the development of the MJO (or at least the convectively active Indian Ocean phase) is favored when warm SST occurs in both the Indian and eastern Pacific Oceans. Comparing the two panels of Fig. 1, we see that the correspondence between the precipitation and SST anomalies is rather complex. The positive precipitation anomalies develop just south of India in the presence of warm SST anomalies (top panels of Fig. 1). For the next 10–15 days the center of the warm precipitation anomalies moves very little (about 10° longitude), while warm SST anomalies develop farther to the east over Indonesia and the Pacific warm pool. At phases -45° and 0° , after the precipitation anomalies have split, the eastern component of the positive precipitation anomalies appear to be linked to (but occur just west of) very localized warm SST anomalies near 165°E longitude.

In Fig. 2, we summarize the relationships between the composite SST anomalies and several other fields using phase–longitude plots. The top-left panel shows that positive SST anomalies tend to occur on the leading edge of (just east of) the main rising branch of the MJO in the Indian Ocean and western Pacific. Our results concerning the forcing of the SST anomalies by latent heat and shortwave flux are generally consistent with previous studies. We find that the latent heat flux anomalies tend to lead the SST anomalies in both the Indian and western Pacific Oceans, with reduced (enhanced) latent heating leading warm (cold) SST anomalies (lower-left panel of Fig. 2). The lag time is somewhat variable but tends to be about 5–10 days. Also, the net

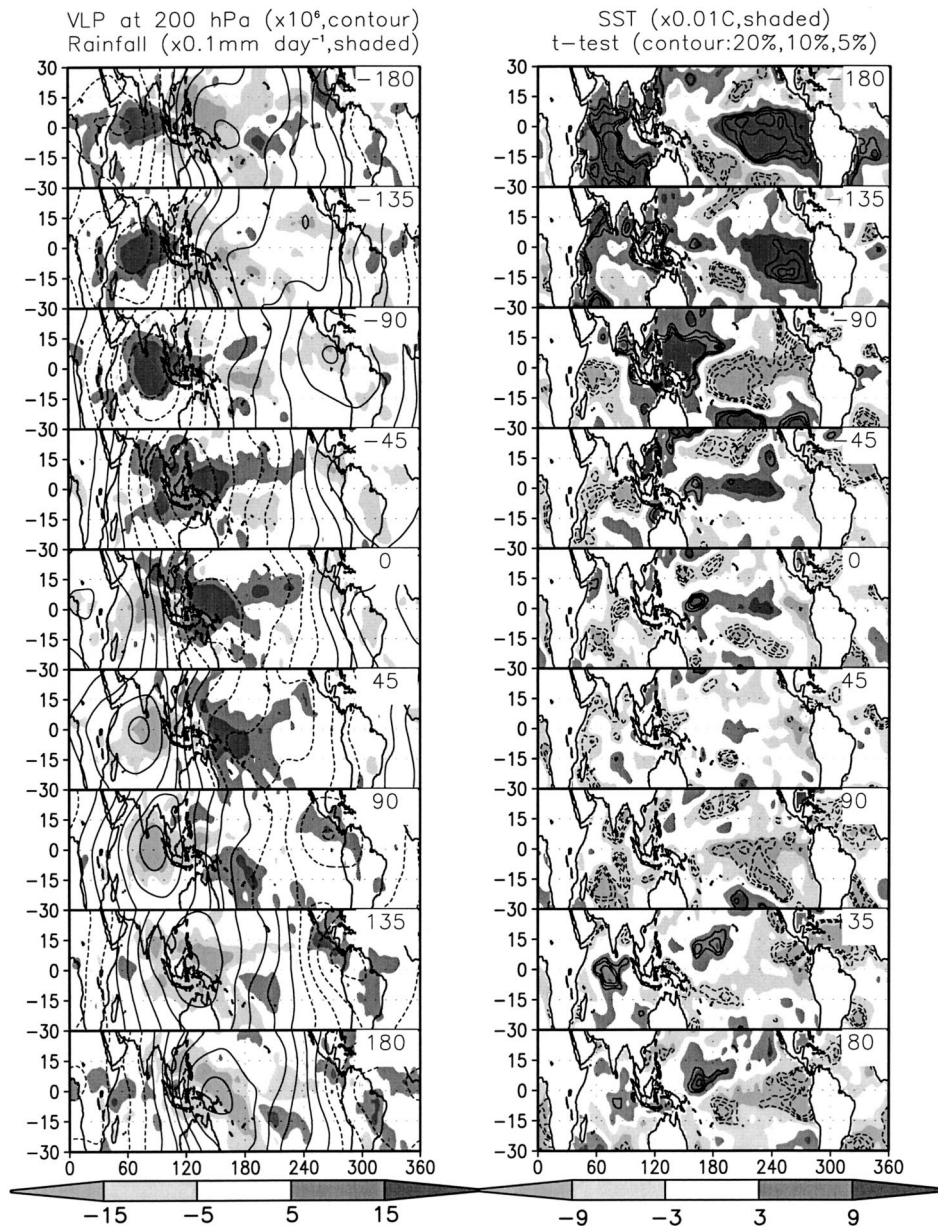


FIG. 1. The composite evolution of the MJO using the leading complex EOF of the filtered (20–70 day) NCEP–NCAR reanalysis 200-mb velocity potential field as an index. The composite evolution goes through a complete cycle (-180° to 180° phase). The results are based on the period 1982–98; values are included in the composite for only those times when the amplitude of the leading EOF is greater than one standard deviation. (left) GPCP precipitation (shaded) and 200-mb velocity potential (contours). (right) SST (shaded) with significance values contoured at 20%, 10%, and 5%. Units for velocity potential are $\text{m}^2 \text{s}^{-1}$.

shortwave flux anomalies are such that enhanced (reduced) shortwave flux leads warm (cold) SST anomalies by 5–10 days (upper-right panel of Fig. 2). It is, however, important to keep in mind that the reanalysis flux quantities are model generated and, therefore, are subject to model bias errors. Shinoda et al. (1999), for example, show that while the NCEP–NCAR reanalysis latent heat fluxes are reasonable, the shortwave fluxes are about half the amplitude of satellite-based estimates

on intraseasonal timescales. In the eastern Pacific Ocean, there is no clear relationship between the SST and either the insolation or the latent heat flux anomalies. The lower-right panel of Fig. 2 shows that the SST anomalies west of 180° tend to lead the main precipitation anomalies supporting the results of Waliser et al. (1999) and others, that suggest a feedback role for the SST in the development of the MJO. In the western Pacific Ocean the lag between the SST and precipitation

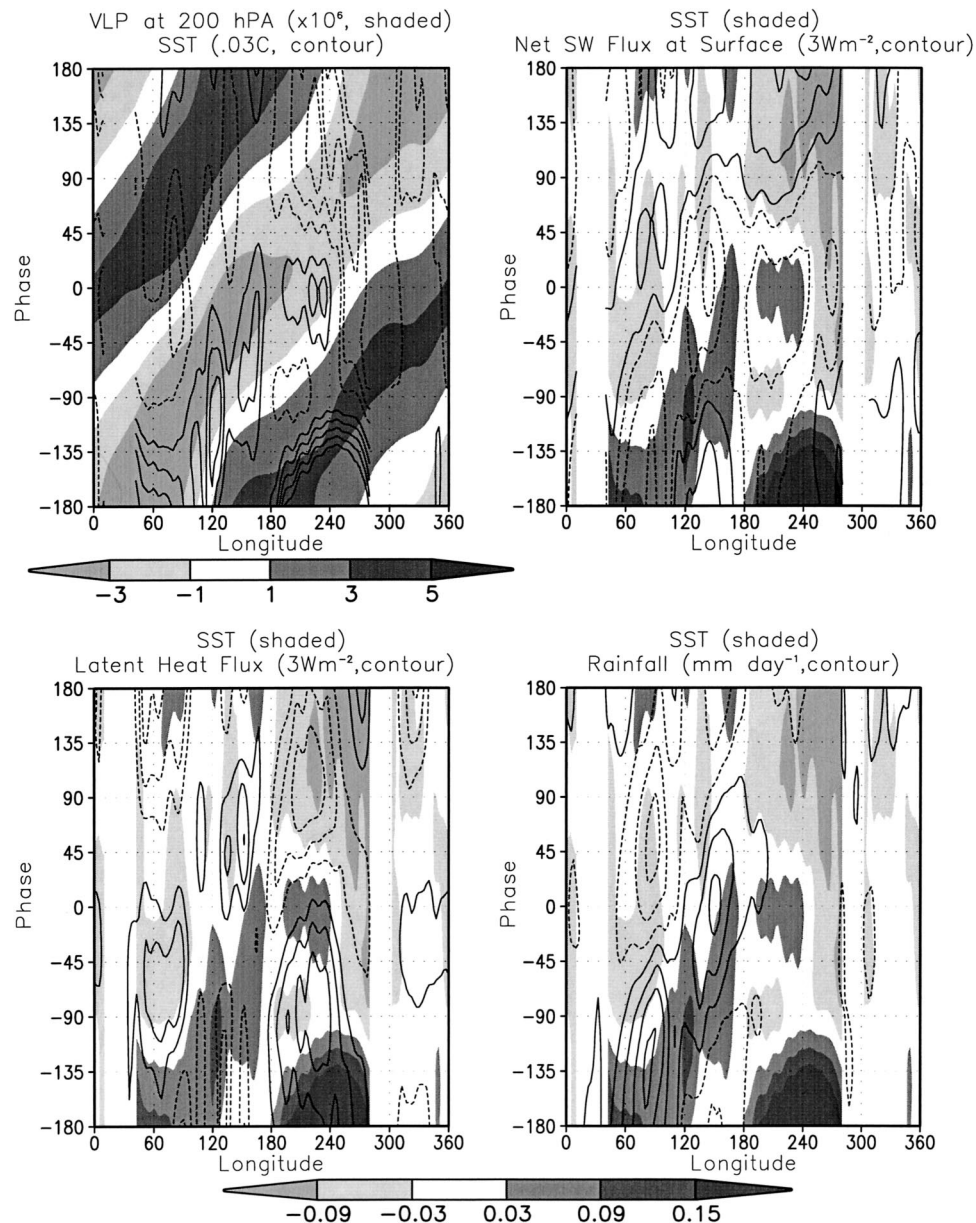


FIG. 2. Same as in Fig. 1, but for phase-longitude diagrams for various fields averaged between 6°S and 6°N . (top left) The 200-mb velocity potential (shaded) and the SST (contours start at $\pm 0.03^{\circ}\text{C}$). Units for velocity potential are $\text{m}^2 \text{s}^{-1}$. (top right) The SST (shaded) and the NCEP-NCAR reanalysis net surface shortwave flux at the surface (contours start at $\pm 3 \text{ W m}^{-2}$). (bottom left) The SST (shaded) and NCEP-NCAR latent heat flux (contours start at $\pm 3 \text{ W m}^{-2}$). (bottom right) The SST (shaded) and the observed precipitation (contours start at $\pm 0.5 \text{ mm day}^{-1}$). The bottom grayshade bar refers to the SST fields.

anomalies appears to be about 10 days, while in the Indian Ocean the lag is about 5 days.

We next look for the signature of the above canonical MJO development during 1997/98 in both the observations and model simulations.

b. Simulated intraseasonal variability for 1997/98

We begin by describing the intraseasonal variability in both the model simulations and the observations for

the period September 1996–August 1998. The basic observed and simulated climatology and the 1997/98 circulation and precipitation anomalies are documented in Kang et al. (2002) and Schubert and Wu (2001), and will not be repeated here. The filtered fields from the simulations are decomposed into forced and free components as described in section 2c(1). While our purpose here is not to highlight differences between the models, we do show how the models compare in the partition of the forced and free variance. For the most part, we

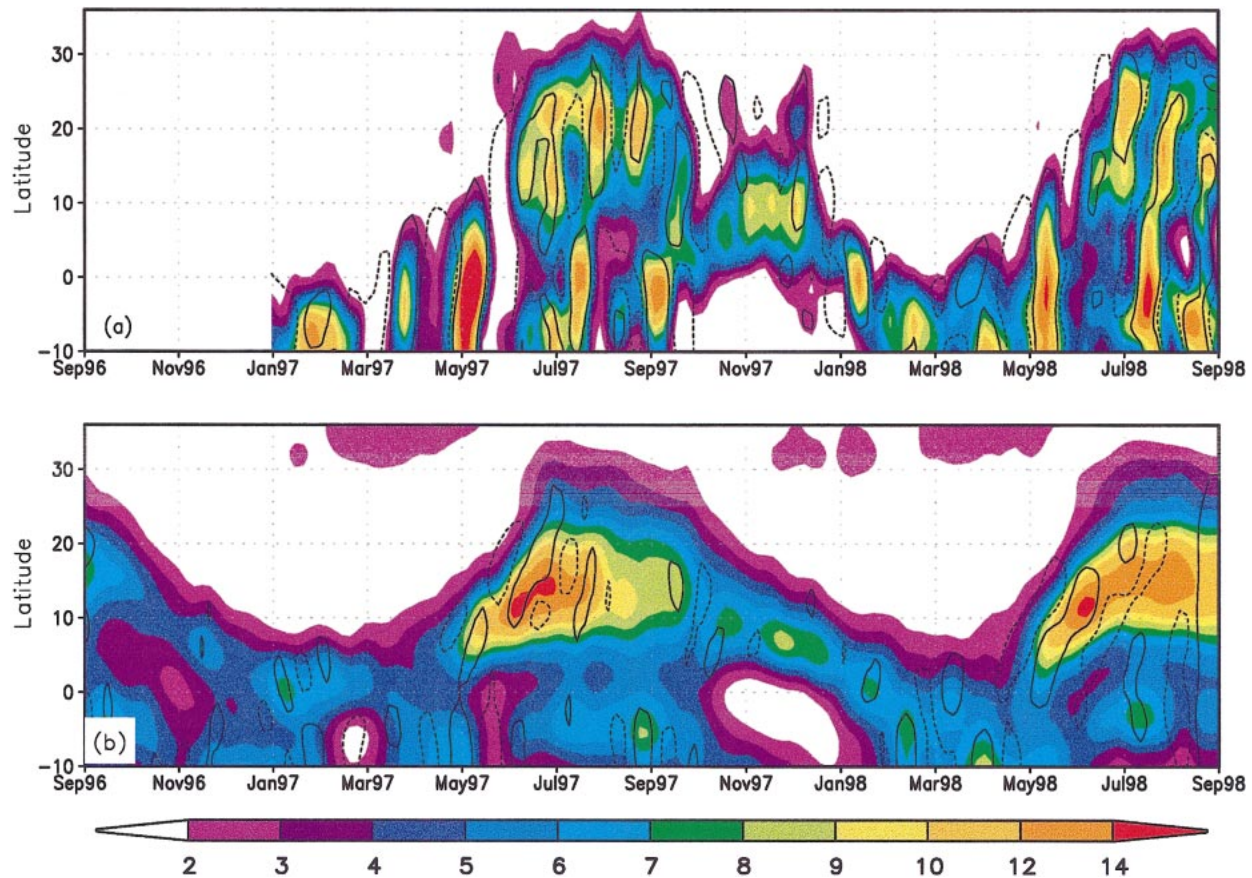


FIG. 3. (a) Latitude–time section of the observed daily precipitation (mm day^{-1}) averaged between 75° and 85°E . Values are only available beginning Jan 1997. The shading denotes the total precipitation and the contours denote the precipitation filtered to retain timescales between 20 and 70 days. (b) Same as (a), but for the ensemble and model mean precipitation. For the filtered data we outline in (a) the $\pm 1 \text{ mm day}^{-1}$ values, and in (b) the $\pm 0.5 \text{ mm day}^{-1}$ values.

focus on the averages over all model simulations allowing us to obtain greater confidence in the significance of the results. One difficulty with this model composite approach is that the models show such a wide range in the simulated intraseasonal variability, that it is unlikely that they represent equally likely estimates of nature.

The important role of intraseasonal variations in the seasonal evolution of the rainfall in the southwest monsoon region is illustrated in Fig. 3 by the total rainfall (shaded) and the rainfall coming from MJO timescales (20–70 days) averaged over the longitudes spanning the Indian subcontinent (75° – 85°E). The observed rainfall (GPCP) is shown in Fig. 3a, and the rainfall obtained by averaging all the simulations is shown in Fig. 3b. The observations show a clear northward progression of the rainfall from the Southern Hemisphere into the Northern Hemisphere that tends to occur on the MJO timescales. For example, the May increase and late May–early June break in the monsoon rainfall during 1997 coincides with the positive and negative rainfall anomalies associated with the MJO timescales. The grand mean of the AGCM simulations (Fig. 3b) shows a similar though more gradual seasonal evolution. This

is, to some extent, to be expected since the results are an average over many cases so that individual MJO events (to the extent that they are simulated by the models) are averaged out. Perhaps the most surprising aspect of Fig. 3b is that there is evidence of MJO variability in the model simulations that is not averaged out (the contours of 20–70-day variability shown in Fig. 3b), but is common to all (or at least many) of the 100 AGCM simulations. This is consistent with the results of Schubert and Wu (2001) based on just one of the AGCMs included here (the GEOS model). The fact that we find such an ensemble mean MJO signal in the grand ensemble and model mean suggests that further study of the nature of this apparently forced variability is warranted.

Figure 4 shows a time–longitude diagram of the unfiltered 200-hPa pentad VLPAs averaged between 5° and 10°N . The NCEP–NCAR reanalysis shows evidence of substantial MJO activity especially during the first half of 1997 when there are well-defined propagating anomalies. The late May–early June Indian monsoon break mentioned earlier is also evident here. During late 1997 and 1998, we see a low-frequency shift that appears to

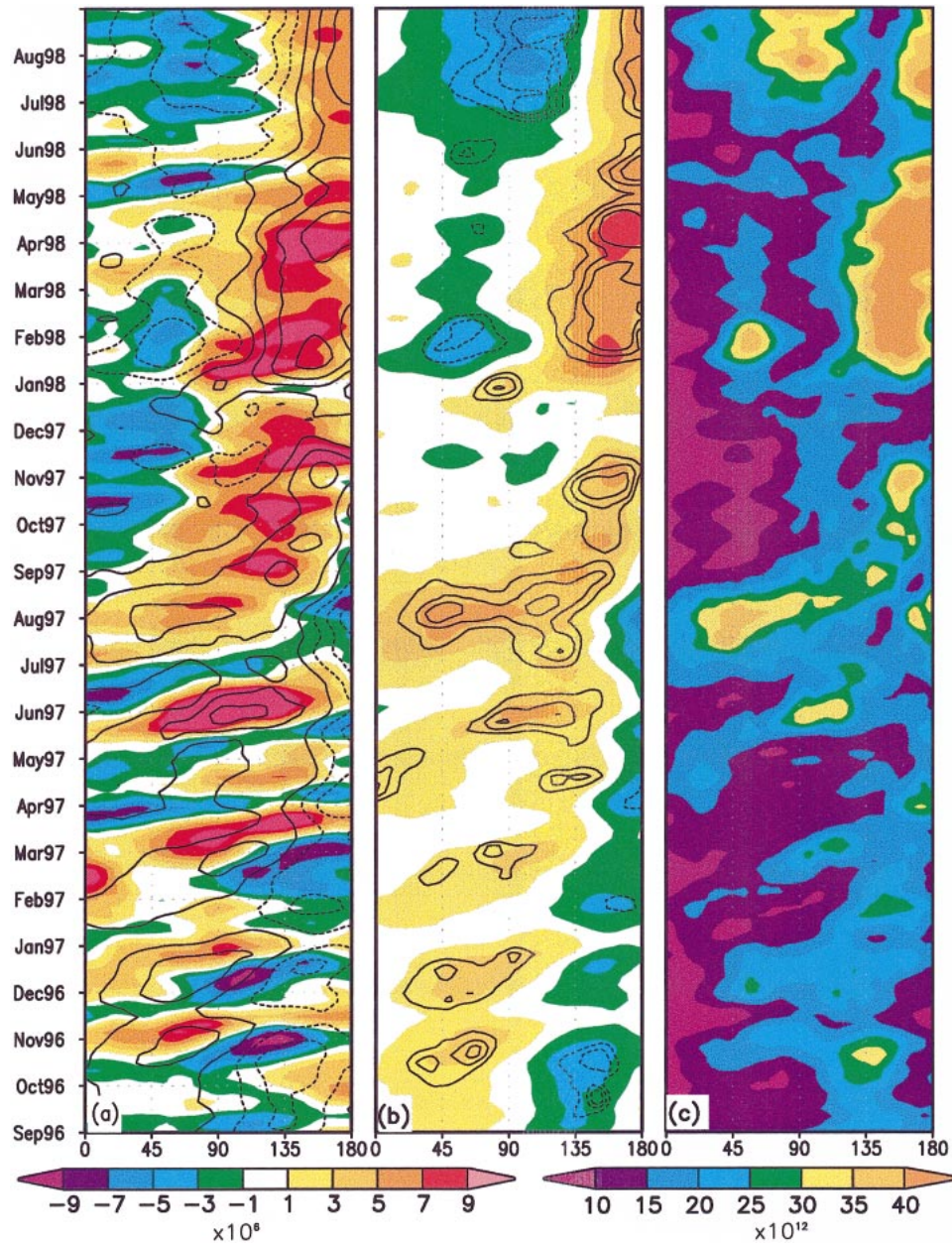


FIG. 4. (a) A longitude–time section of the NCEP–NCAR reanalysis 200-mb velocity potential unfiltered pentad anomalies averaged between 5° and 10°N . The contours are the same quantity, except for the ensemble and model mean anomaly fields. (b) A repeat of the ensemble and model mean anomaly fields with superimposed contours of three significance levels (20%, 10%, and 5%). (c) The intraensemble variance (averaged over all models) of the filtered (20–70 day) 200-mb velocity potential anomalies averaged between 5° and 10°N . Units are $\text{m}^2 \text{s}^{-1}$ for the mean and $(\text{m}^2 \text{s}^{-1})^2$ for the variance.

be the signature of the developing ENSO. There is also evidence of MJO variability during the spring and summer of 1998 [though with somewhat shorter timescales compared with 1997; see also Schubert and Wu (2001)]. The ensemble and model-mean unfiltered pentad VLPAs (deviations from each model's pentad climatology) are superimposed as contours in Fig. 4a and repeated in color in the Fig. 4b. The three contour levels in Fig. 4b

indicate the regions where the ensemble mean values are significant at the 20%, 10%, and 5% level, based on a t test. The simulated VLPAs display significant MJO signals that occur at approximately the time when major events occurred in nature. The ensemble mean of the simulated events, however, are weaker than the anomalies found in the reanalysis. They also tend to lead; in fact, they tend to be in quadrature with, the

observed anomalies. We will return to the issue of the phasing of the events in the next section. These results are consistent with the results from the GEOS model reported in Schubert and Wu (2001), and suggest that the models are responding to the intraseasonal variability in the specified weekly SST observations.

Figure 4c shows the evolution of the 20–70-day filtered intraensemble or free variance, s_g^2 (averaged over all models). This shows that enhanced free variability in the velocity potential tends to coincide with periods during which enhanced ensemble mean velocity potential anomalies occur. This is particularly evident in 1998 when there is a substantial increase in the free variability east of about 120°W in a region of positive ensemble mean anomalies (associated with an ENSO-related shift in the Walker circulation). After June 1998, there is also an increase in variability west of 120°W coinciding with the development of negative ensemble mean anomalies over the eastern Indian Ocean.

Figure 5 shows maps of the total 20–70-day filtered intraseasonal variance simulated by each model and compares them with the results from the NCEP–NCAR reanalysis. We see that the models exhibit a wide range of variability. On one extreme is the IAP model that shows variability more than twice that of the reanalysis throughout the Tropics. On the other end of the spectrum is the DNM model, which has variance about a factor of 10 less than that of the reanalysis. The GFDL model appears to be closest to the reanalysis showing variability that is similar to the reanalysis in both magnitude and spatial distribution.

We next partition the simulated filtered intraseasonal variability into forced (variance of the ensemble mean) and free (intraensemble variance) components as described in section 2c(1). The results, shown in Fig. 6, indicate that for all the models the free variance dominates the intraseasonal filtered variability. All the models have forced variability that is largest over the eastern Indian Ocean and the western Pacific Ocean. Again, there are, however, substantial differences between the models in both the magnitude and in the partition of the forced and free variability. The SUNY–GLA model has the largest forced variability while the DNM model has the weakest. The large IAP model variability mentioned earlier is mostly in the free component. The partition of the variance is seen more clearly in Fig. 7, which shows, in the left panel, the ratio of the forced to total filtered variability (P_β) and, in the right panel, the ratio of the forced to free filtered variability (U). The SUNY–GLA and DNM models have the largest values of P_β with values exceeding 30% over parts of the eastern Indian Ocean and/or the western Pacific Ocean. The MRI, NCAR, and SNU models also have substantial fractions of the variability in the forced component with values of P_β exceeding 20% over much of the western Pacific and Indian Oceans. The two models with the most realistic total variance (see Fig. 5) show considerable differences in P_β , with the GFDL model showing

values that are generally less than 20%, compared with more than 30% for the SUNY–GLA model. More than half of the models have signal (the forced response) to noise ratios (U) that are greater than 30%.

c. A case study

In this section, we examine in some detail a particular MJO event that occurred during the spring of 1997. Figure 8 shows the time series of the simulated and reanalysis filtered 200-mb velocity potential and the SST for a region in the tropical Indian Ocean. Here we have changed the sign on the VLPAs to show more clearly the phasing with the SST anomalies. All the time series show substantial intraseasonal oscillations during the first half of 1997. The reanalysis and simulated VLPAs appear to be synchronized with each other and with the SST anomalies though the exact phasing appears to change somewhat with time. The model simulations show VLPAs that are strongly coupled with the SST anomalies, with warm SST anomalies associated with negative VLPAs. The reanalysis velocity potential also shows a link to the SST though at times it is nearly in quadrature with the SST (e.g., during September–October and during April 1997), consistent with the picture presented in section 3a, and in earlier studies of clear skies (positive VLPAs) and reduced winds leading to a warmer ocean (e.g., Jones et al. 1998). To better understand these relationships we next focus on the MJO event that occurred during the time period 12 February–12 May 1997. This event was chosen because it is one of the most pronounced oscillations to occur during these two years, and it is not immediately preceded by other large events that could introduce SST anomalies that persist into the next event. We therefore hope to obtain a clearer picture of the link between the development of SST anomalies and the MJO.

The left panel of Fig. 9 shows the filtered (20–70 day) SST anomalies (deviations from the 1982–98 climatology) averaged every 10 days. While the field is somewhat noisy, there is evidence, beginning in February, of eastward propagation of the cold anomalies from the Indian Ocean into the western Pacific. Also, the warm SST anomalies that develop over the western Indian Ocean at the beginning of March appear to propagate into the western Pacific in about 40 days. The propagation of the anomalies is shown more clearly in the Hovmoeller diagram of the SST within $\pm 10^\circ$ of the equator (right panel of Fig. 9).

The simulated and reanalysis filtered 200-mb VLPAs for that period are shown in Fig. 10. The simulated results (left panel) are the average over all ensemble members and models (the forced component). The simulations show a coherent time evolution, with a dipole structure developing over the Indian Ocean and Indonesia that has a spatial-scale consistent with about a wavenumber-2 structure, which then strengthens and propagates slowly (about 5 m s^{-1}) to the east. A com-

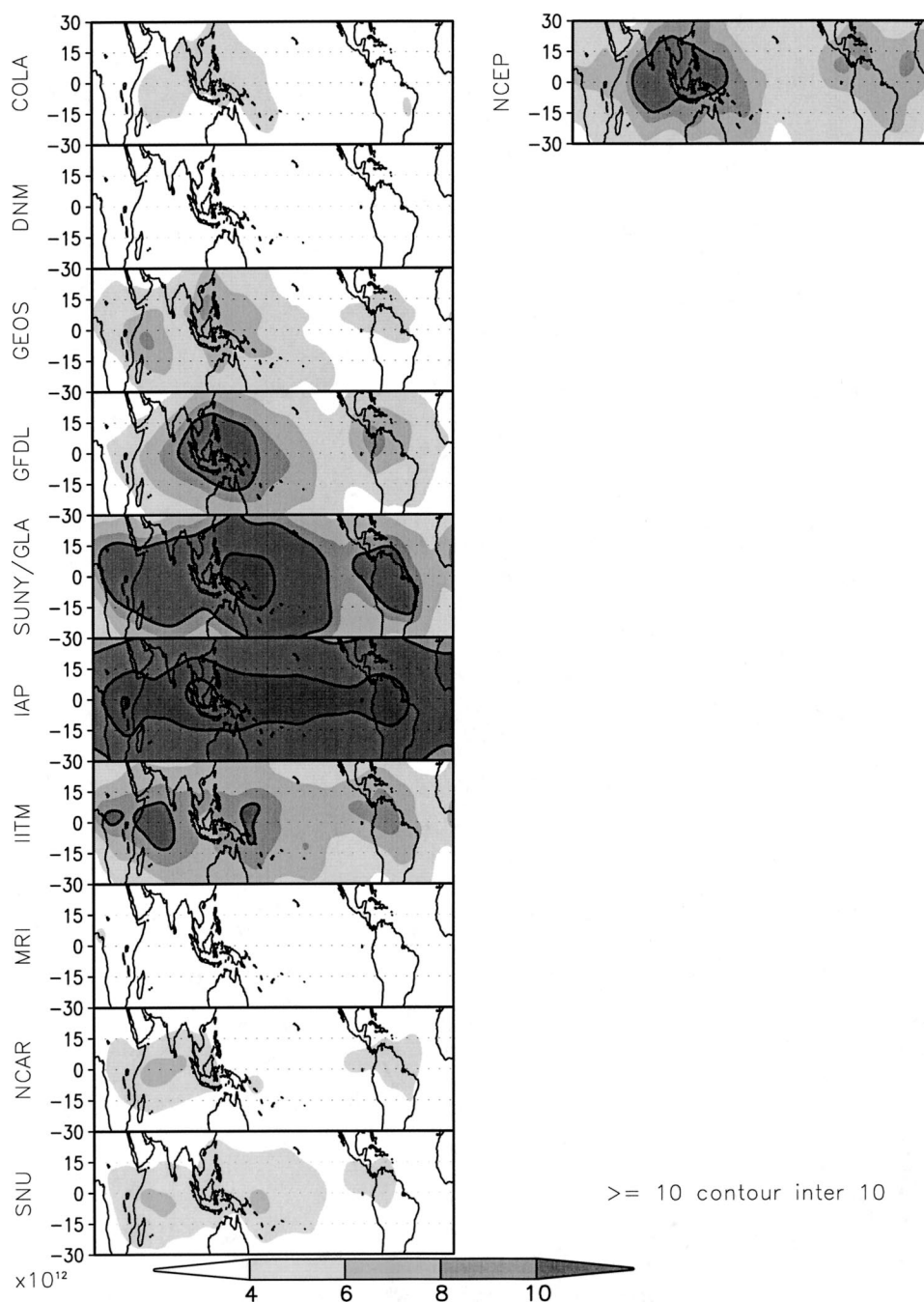


FIG. 5. The total variance of the filtered (20–70 day) 200-mb velocity potential for (left) each model and (right) the NCEP–NCAR reanalysis for the time period Sep 1996–Aug 1998. Units are $\text{m}^4 \text{s}^{-2}$.

parison with the SST anomalies in Fig. 9 shows that the development is roughly consistent with the SST in the sense that anomalous rising motion tends to coincide with warm SST anomalies and anomalous sinking motion tends to coincide with cold SST anomalies (see also Fig. 8). The reanalysis shows a qualitatively similar evolution, starting also as a wavenumber-2 dipole over the Indian Ocean and the central Pacific and propagating to

the east, though after about 30 days it evolves into a zonal wavenumber-1 structure characteristic of the MJO. Figure 10 also shows that the simulated and observed anomalies are not in phase, but tend to be in quadrature with the simulations leading the observed anomalies in the Eastern Hemisphere. In fact, if one were to shift the simulated anomalies about 10 days back (one panel in Fig. 10), the observed and simulated

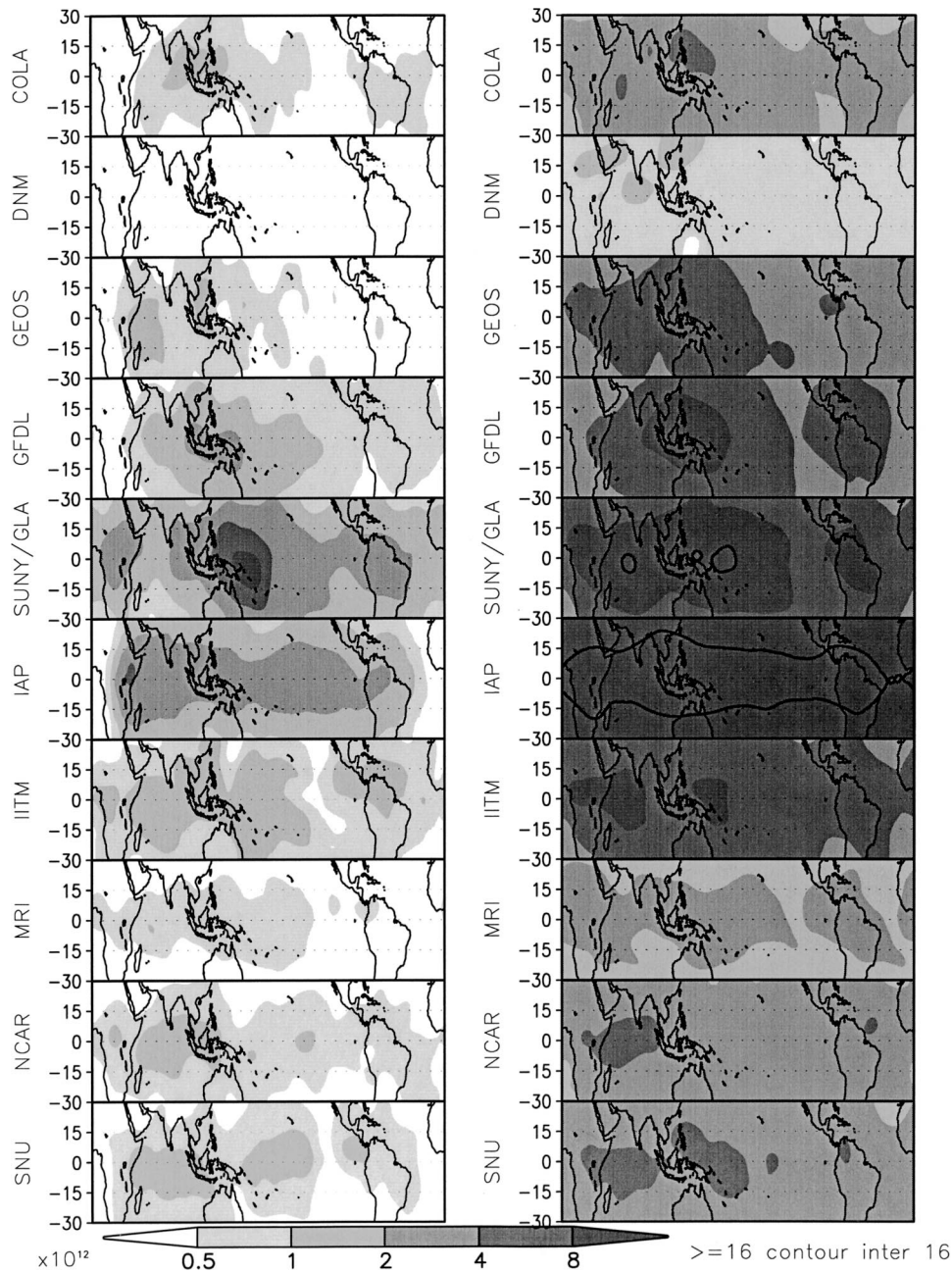


FIG. 6. (left) The forced (interensemble) variance of the filtered (20–70 day) 200-mb velocity potential for each model. (right) The free (intraensemble) variance of the filtered (20–70 day) 200-mb velocity potential for each model. Units are $\text{m}^4 \text{s}^{-2}$.

anomalies would be nearly in phase throughout much of the Eastern Hemisphere. This is quantified in Fig. 11, which shows the lag correlations between the simulated and observed anomalies. This shows that the largest positive correlations (>0.90) occur over the Indian Ocean when the simulated anomalies lead the observed by 10 days. An examination of the correlations between the observed and the ensemble mean simulations for each model (not shown) indicates that the phase lag in

the convectively active regions is fairly robust, with values ranging between about 5 and 15 days. Over the western Pacific Ocean, the simulated anomalies lead by about 5 days. Since the anomalies oscillate in time, negative correlations tend to occur at opposite (positive) lags.

While the reanalysis shows the anomaly propagating around the globe, the simulated ensemble mean anomalies are largely confined to longitudes west of about

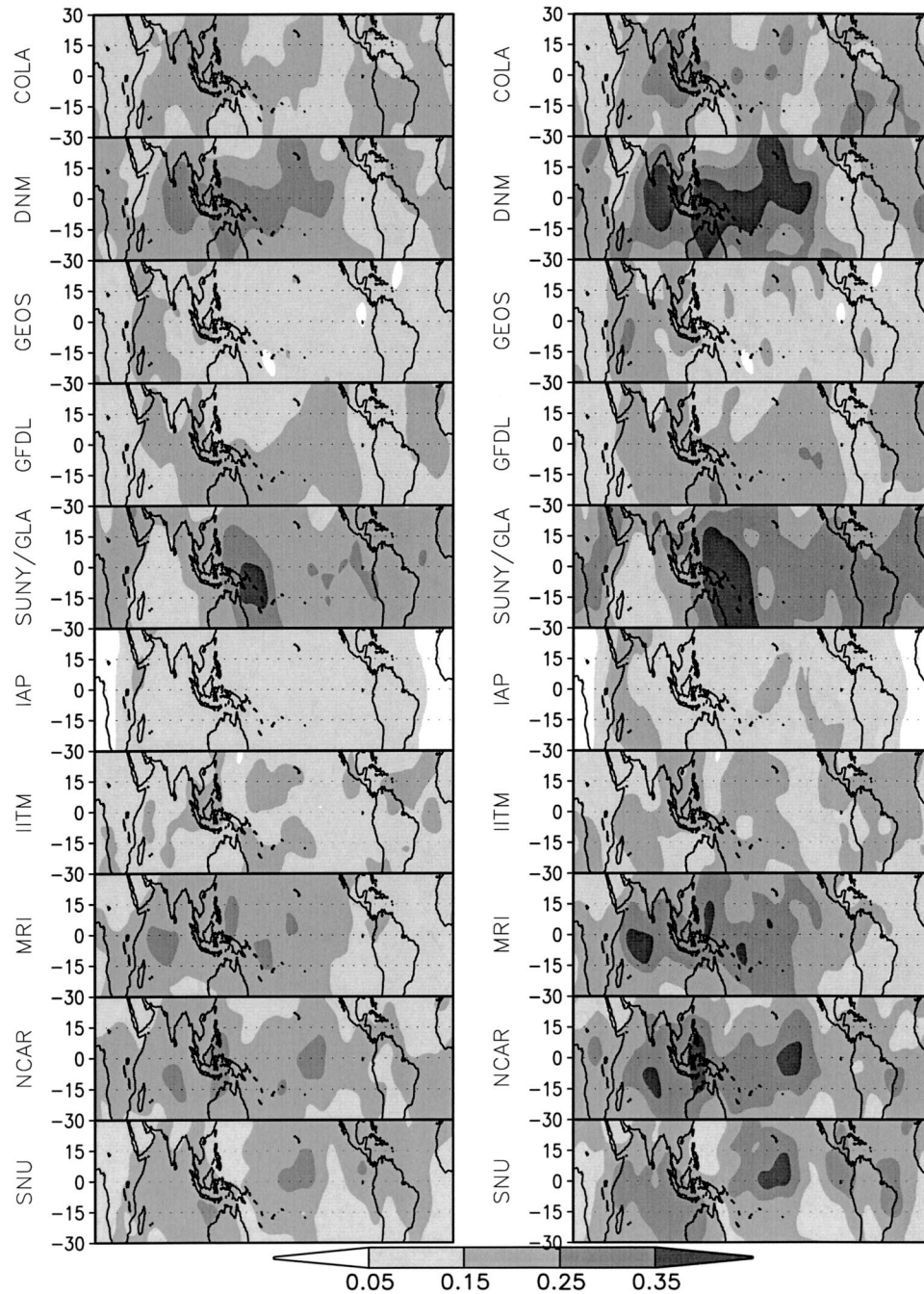


FIG. 7. (left) The ratio of the forced (interensemble) to total variance of the filtered (20–70 day) 200-mb velocity potential for each model (P_β). (right) Same as the left but for the ratio of the forced (interensemble) to free (intraensemble) variance (U).

120°W. As we shall see next, this reflects the strong link between the ensemble mean velocity potential and SST anomalies in the Indian and western Pacific Oceans. Note that the mean simulated anomalies are about a factor of 3 or 4 smaller than the reanalysis anomalies. This is presumably in part due to the averaging process: the anomalies from the reanalysis represent a single realization (including both forced and free components).

Outside the convectively active region, the simulated variability is primarily free and the averaging tends to cancel out the anomalies from the various runs: we will discuss the nature of the free variability later in this section.

Figure 12 is the same as Fig. 10, except for the precipitation anomalies. The superimposed contours are a repeat of the VLPAs from Fig. 10. The results show a

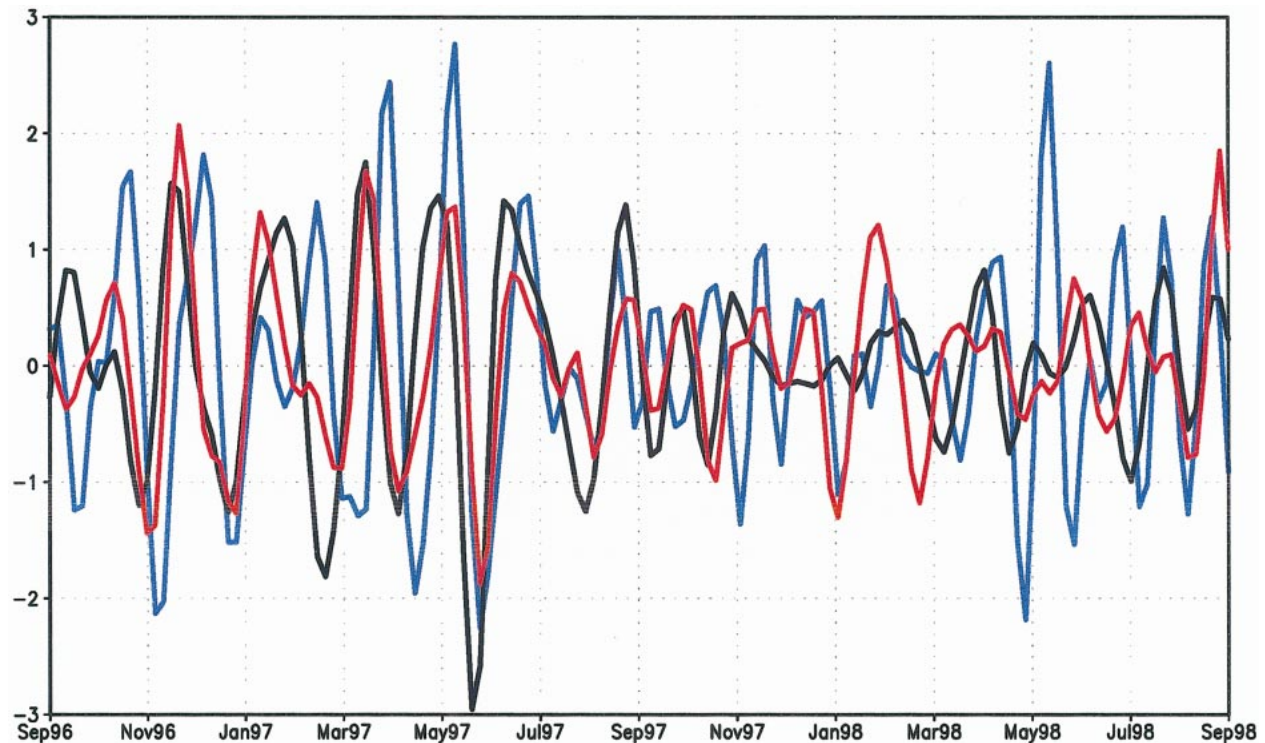


FIG. 8. Time series of the 20–70-day filtered 200-mb velocity potential (multiplied by -1) and SST anomalies averaged from 10°S – 10°N to 60° – 100°E . The red curve is the ensemble and model mean velocity potential. Multiply values by 1.0×10^6 to get units of $\text{m}^2 \text{s}^{-1}$. The blue curve is the NCEP–NCAR reanalysis velocity potential. Multiply values by 3.3×10^6 to get units of $\text{m}^2 \text{s}^{-1}$. The black curve is the SST in units of 0.1°C .

strong relationship between the precipitation and VLPAs, especially for the simulations. For example, in the beginning of March both the models and the reanalysis show enhanced precipitation south of the equator near the date line and generally reduced precipitation to the west. Both the simulations and the model show a local zonal wavenumber-2 velocity potential “response” to the precipitation anomalies. Subsequently, the reanalysis VLPAs propagate eastward and appear to decouple from the rainfall anomalies, and develop into a wavenumber-1 structure. The mean simulated anomalies, on the other hand, remain in lock step with the precipitation anomalies. The simulated mean precipitation anomalies in the Indian Ocean and western tropical Pacific (left panel of Fig. 12) appear to be strongly linked to the SST anomalies (Fig. 9). The observed precipitation anomalies (right panel of Fig. 12), show less of a direct spatial coherence with the SST anomalies, especially over the Indian Ocean.

While the previous results focused on the ensemble mean forced response to the SST, we can also examine the structure of the free (intraensemble) variability during the 12 February–12 May time period. We accomplish this by computing the intraensemble variance and its time lag correlations. In particular, we compute the lag correlations between the free (intraensemble) fluctuations in the 200-mb velocity potential at a base region

(an average over the region 15°S – 10°N , 80° – 110°E and a base time (the 10-day average of 24 March–2 April), with the free fluctuations in the velocity potential at all grid points and other times. We compute an “all model” lag correlation by averaging the covariances and variances over all the models before dividing to compute a correlation.

The evolution of the intraensemble variance (left panel of Fig. 13) shows a general increase in time over Indonesia and the western Pacific through 3 April, followed by a decline. Over Africa and the Indian Ocean, the variance is largest during April, whereas over South America it peaks at the beginning of March. There does not appear to be a strong correspondence between the evolution of the signal (Fig. 12) and the intraensemble variance in Fig. 13. The lag correlation results (right panel of Fig. 13) provide a picture of the spatial structure and evolution of the free variability that is different from that of the forced response shown in Fig. 10 (left panel). Instead of the slowly propagating, predominantly local wavenumber-2 pattern in the Western Hemisphere, the free variability is characterized by a faster propagating (about 10 – 15 m s^{-1}) zonal wavenumber-1 structure that is more reminiscent of the behavior of the observed MJO away from the convectively active regions of the western Pacific and Indian Oceans (cf. right panel of Fig. 10). Note that the fact that we obtain a coherent

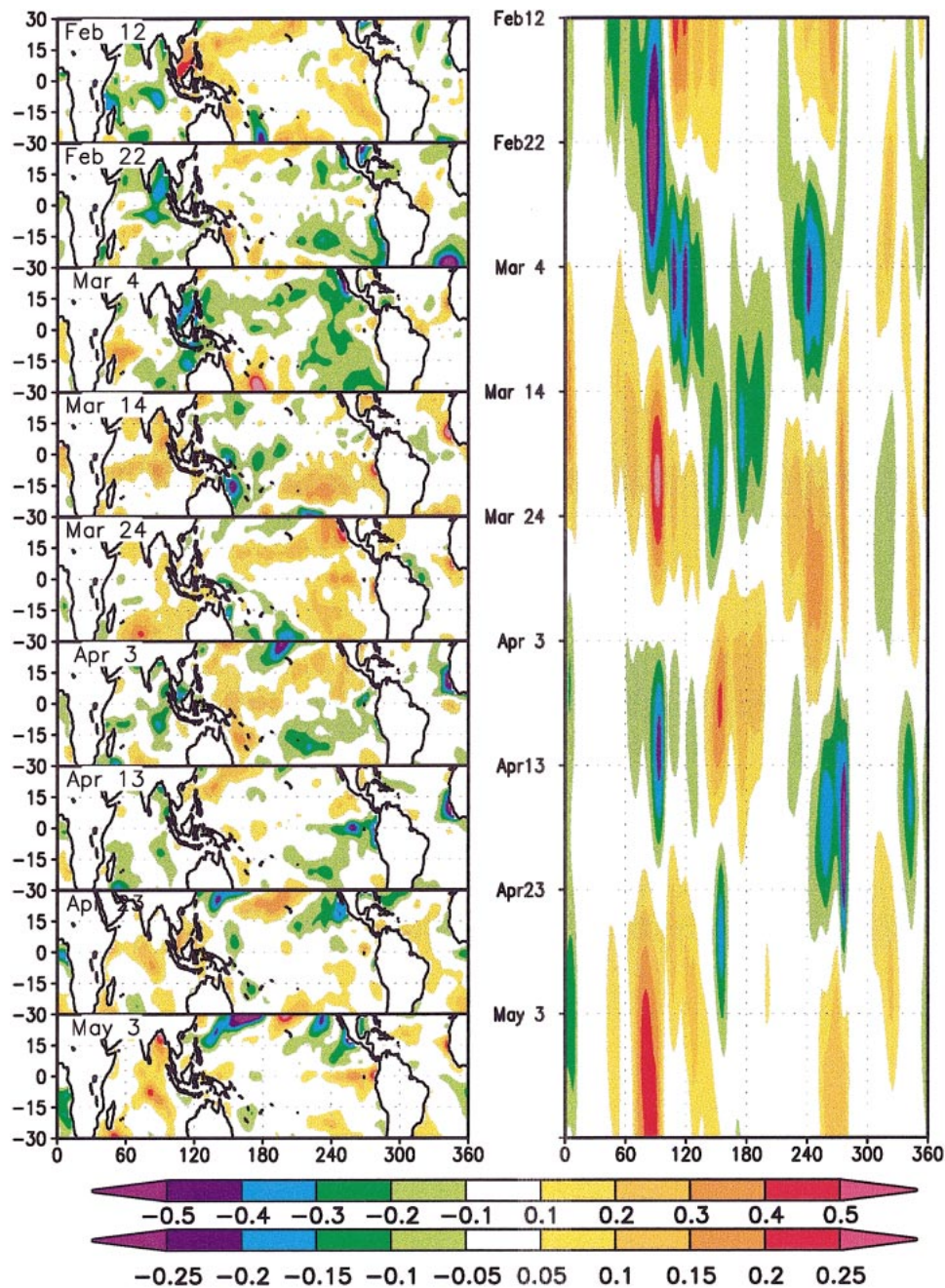


FIG. 9. (left) Ten-day averages of the filtered (20–70 day) SST anomalies for the period 12 Feb–12 May 1997. (right) Hovmöller diagram of the SST within $\pm 10^\circ$ of the equator. Lower color bar is for the right panel. Units are $^\circ\text{C}$.

lag correlation signal at all, suggests that the free variability must be, to some extent, synchronized with the forced response (though it could be of either sign). We have also computed the EOFs of the free variability for this time period (not shown), and found that the leading modes have a structure that is very similar to that shown in the right panel of Fig. 13. In those calculations, the EOFs were computed from the extended correlation ma-

trix that includes all pentads between 12 February and 12 May 1997.

The above results show that the free and forced variations have substantially different characteristics. The free variability is similar in structure and phase speed to the observed MJO away from the convectively active regions of the western Pacific and Indian Oceans. The forced response, on the other hand, is largely confined to the con-

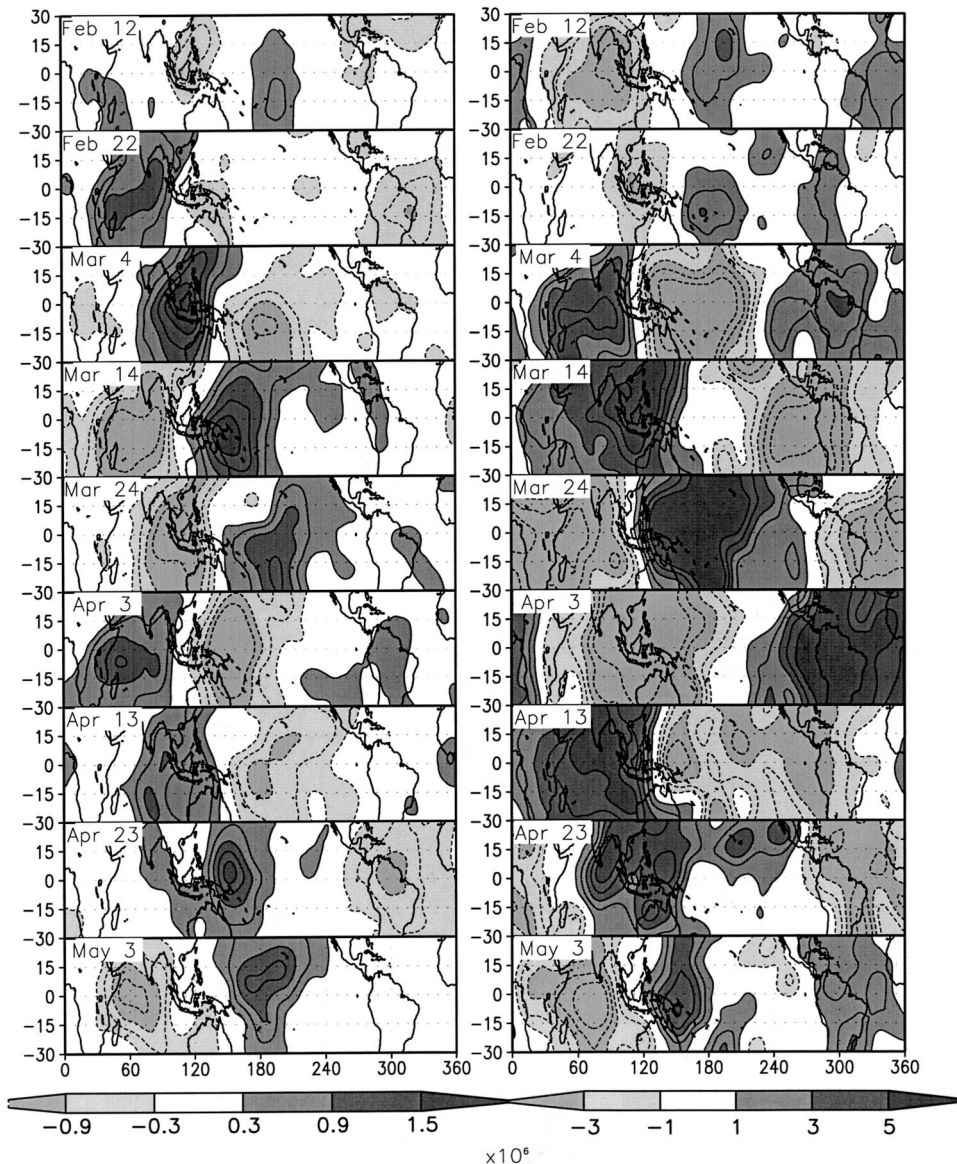


FIG. 10. (left) Ten-day averages of the filtered (20–70 day) ensemble and model mean 200-mb velocity potential field for the period 12 Feb–12 May 1997. (right) Ten-day averages of the NCEP–NCAR reanalysis filtered (20–70 day) 200-mb velocity potential anomalies for the period 12 Feb–12 May 1997. The reanalysis anomalies are computed as deviations from the 1982–98 climatology of 10-day averages. Units are $\text{m}^2 \text{s}^{-1}$.

vectively active regions, and tends to lead the observed MJO by about 10 days. This appears to reflect the fact that in nature, warm SST anomalies develop ahead of the MJO's main convective center, while the cold anomalies develop behind it (Fig. 2). In the model simulations, the response is, however, in phase with the SST, and one might argue that this response is indicative of the feedback to the SST that occurs in nature on, for example, the leading edge of the convective center of the MJO.

4. Summary and conclusions

There is growing observational and theoretical evidence that the atmospheric MJO is part of a coupled

atmosphere–ocean phenomena (e.g., Zhang 1996; Hendon and Glick 1997; Wang and Xie 1998; Jones et al. 1998). This is bolstered by recent studies employing AGCMs coupled to mixed-layer ocean models that note improved simulations of the MJO (Flatau et al. 1997; Waliser et al. 1999). The results are, however, model dependent and the degree of improvement (and possibly the mechanisms involved) appear to depend on the differing capabilities of the uncoupled AGCMs to simulate the MJO (Hendon 2000).

This study took a somewhat different approach to addressing the MJO–SST coupling issue by examining whether AGCMs run with prescribed SSTs exhibit a

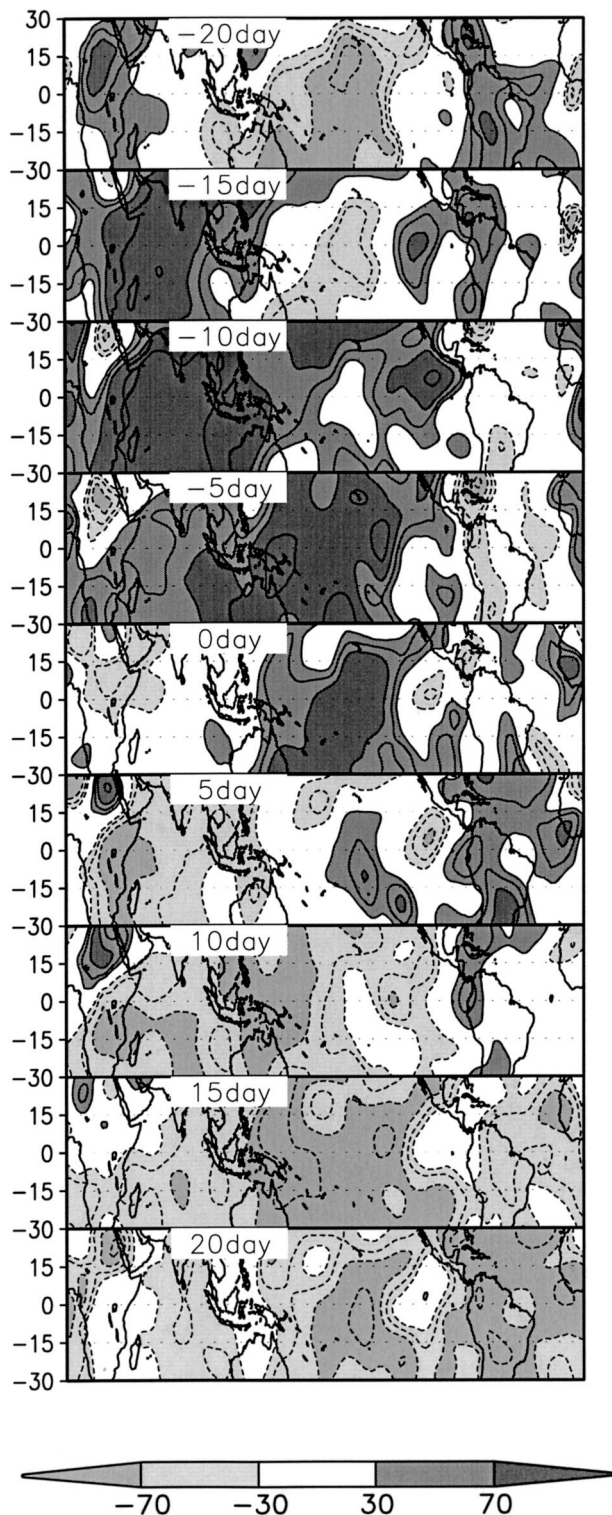


FIG. 11. Lag correlations between the filtered (20–70 day) ensemble/model mean and the observed (reanalysis) 200-mb velocity potential anomalies computed over for the period 12 Feb–12 May 1997. Negative lags indicate the simulated anomalies lead the observed anomalies.

significant atmospheric response to the SST on intraseasonal timescales. In light of the strong model dependence of the results noted above, we employed ensembles of simulations produced by 10 different AGCMs. These runs were produced using observed weekly SSTs for the 2-yr period 1997/98 as part of the Asian–Australian Monsoon AGCM intercomparison project sponsored by the World Climate Research Program/CLIVAR Asian–Australian Monsoon panel (Kang et al. 2002).

The analysis involved decomposing the 20–70-day variability into forced (interensemble) and free (intraensemble) components. The results showed considerable differences among the models in the representation of the 20–70-day velocity potential variability at 200 mb, ranging from much weaker to much larger than the observed variance. A key result is that the models do produce, to varying degrees, an ensemble mean response to the imposed weekly SST. The forced variability in the models tends to be largest in the Indian and western Pacific Oceans, and occurs primarily during periods of strong observed MJO activity. For some models, the forced (interensemble) variations account for more than a quarter of the 20–70-day intraseasonal variability in the upper-level velocity potential during these two years.

A case study of a strong MJO event showed that the models produce an ensemble mean eastward-propagating signal in the tropical precipitation field over the Indian Ocean and western Pacific, similar to that found for the MJO event in the observations. The associated forced 200-mb VLPAs are strongly phase locked with the precipitation anomalies, propagating slowly to the east (about 5 m s^{-1}) with a local zonal wavenumber-2 pattern that is generally consistent with the developing MJO found in the observations. A comparison of the phases of the two phenomena, however, shows that they are approximately in quadrature, with the simulated response leading the observed by 5–10 days. The phase lag occurs because, in the observations, the positive SST anomalies develop upstream of the main convective center in the subsidence region of the MJO, as a result of reduced latent heat flux and increased net surface insolation. In the simulations, the forced component is in phase with the SST so that the simulated convection and VLPAs lead those of the observations by 5–10 days.

For all the models examined here, the intraseasonal variability is dominated by the free (intraensemble) component. Increases in the magnitude of the free variability tend to coincide with periods during which the forced response is strongest. The results of our case study show that the free variability has a zonal wavenumber-1 pattern, and has propagation speeds ($10\text{--}15 \text{ m s}^{-1}$) that are faster than those of the forced component, and more typical of observed MJO behavior away from the convectively active regions. Furthermore, we found that the free variability appears to be synchronized with the forced response, at least, during the strong event studied here. The above results are significant

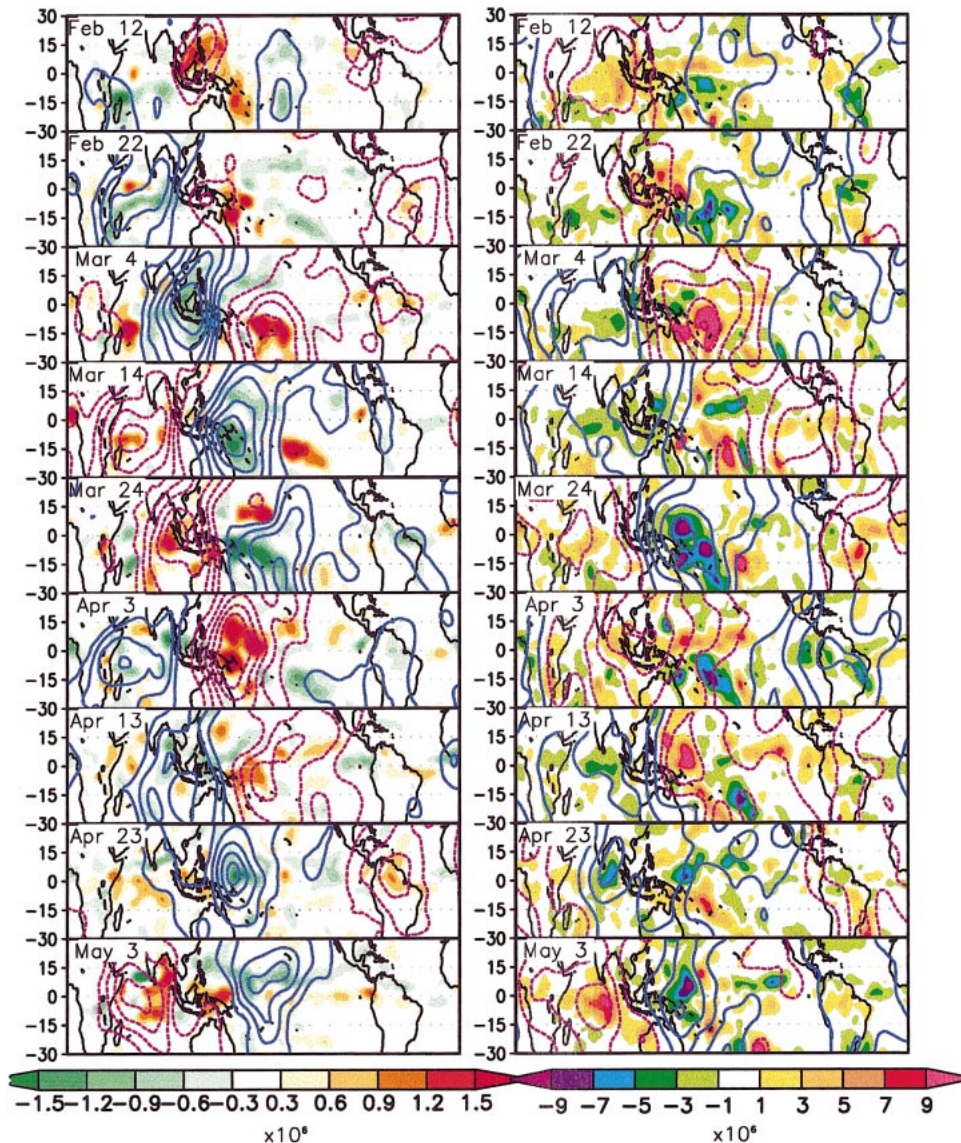


FIG. 12. Same as Fig. 10, but for precipitation (shading) and a repeat of the 200-mb velocity potential (contours, blue are negative values). (left) Values are the ensemble and model mean. (right) Values are the GPCP precipitation and NCEP–NCAR reanalysis 200-mb velocity potential. Units for precipitation are mm day^{-1} . Contour intervals for 200-mb velocity potential are, for the model results $\pm 0.3, 0.6, 0.9, 1.2, 1.5 \times 10^6 \text{ m}^2 \text{ s}^{-1}$, and for the reanalysis $\pm 1, 3, 5, 7, 9, 11 \times 10^6 \text{ m}^2 \text{ s}^{-1}$.

because, despite the lack of a direct link of the free variability with the SST, the synchronization of the intraseasonal variability with the forced response provides hope that we may nevertheless be able to predict some aspects of the free component based on the SST.

The extent to which the ensemble/model mean simulated response to prescribed SSTs provides a reasonable estimate of the magnitude of the true SST feedback on the MJO is unclear. It is, of course, possible that the SST feedback in the coupled problem is substantially different from the response to prescribed SSTs. In fact, the phase difference between the forced response in the models and the response estimated from the observa-

tions suggests this may be the case. On the other hand, one could argue that the phase difference is not inconsistent with an SST feedback that occurs on the leading edge (and is a small fraction) of the main convective anomaly of the MJO. Nevertheless, we suggest that our analysis provides a reasonable estimate of the magnitude of the feedback in the coupled problem, subject to model errors as discussed below. This issue could be examined in future studies by comparing AGCM runs in which the same model is run in both coupled and uncoupled modes. The phase difference also suggests that one must be careful in the interpretation of tropical variability that exists in AGCM simulations with prescribed SSTs,

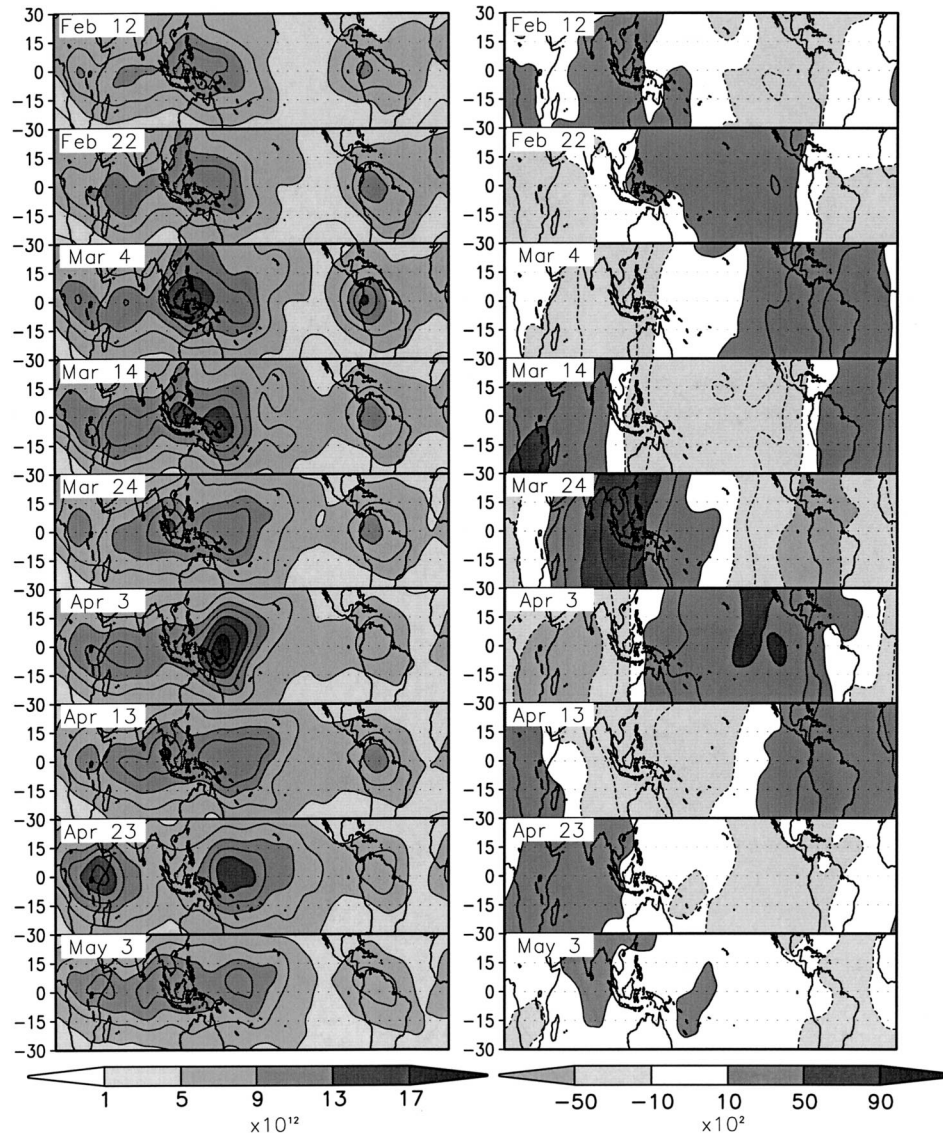


FIG. 13. (left) The intraensemble variance of the 200-mb velocity potential averaged over all models. (right) The time lag correlations ($\times 100$) of the 200-mb velocity potential. The base period is the 10-day-average period 24 Mar–2 Apr 1997 (15°S – 10°N , 80° – 110°E). The lag correlations are computed between the base region and all other grid points and 10-day-averaged time lags ($\pm 0, 10, 20, 30, 40$ days) over all ensemble members and models. See text for details.

when those SSTs contain timescales short enough to resolve the MJO.

Finally, the large range in the variability among the 10 models in both the relative (P_{β}) and absolute value of the forced response shows that current convective schemes vary considerably in their sensitivity to SSTs, and indicates that the schemes have not yet converged on the correct response (see also Slingo et al. 1996). It is noteworthy that even for the two models with the most realistic intraseasonal variability (GFDL and SUNY–GLA), there are considerable differences in both the magnitude and distribution of the forced variability. Nevertheless, these results support the idea that coupling

with SSTs plays an important, though probably not dominant, role in the MJO. The magnitude of the response of the atmosphere to SSTs appears to be in the range of 15%–30% of the total intraseasonal (20–70 day) variability over much of the tropical eastern Indian and western Pacific Oceans.

Acknowledgments. Yehui Chang kindly provided the code for the complex EOF calculation. This work was supported by the NASA Earth Science Enterprises's Global Modeling and Analysis Program, and is a contribution to the CLIVAR/Monsoon GCM intercomparison project. Support for D. Waliser was provided by

the Atmospheric Sciences Division of the National Science Foundation under Grant ATM-9712483.

REFERENCES

- Chang, Y., S. D. Schubert, S. J. Lin, S. Nebuda, and B.-W. Shen, 2001: The climate of the FVCCM-3 Model. NASA Tech. Memo. 104606, Vol. 20, 127 pp.
- Flatau, M., P. J. Flatau, P. Phoebus, and P. P. Niiler, 1997: The feedback between equatorial convection and local radiative and evaporative processes: The implications for intraseasonal oscillations. *J. Atmos. Sci.*, **54**, 2373–2386.
- Hendon, H. H., 2000: Impact of air–sea coupling on the Madden–Julian oscillation in a general circulation model. *J. Atmos. Sci.*, **57**, 3939–3952.
- , and M. L. Salby, 1994: The life cycle of the Madden–Julian oscillation. *J. Atmos. Sci.*, **51**, 2225–2237.
- , and J. Glick, 1997: Intraseasonal air–sea interaction in the tropical and Pacific Oceans. *J. Climate*, **10**, 647–661.
- Huffman, G. J., R. F. Adler, M. M. Morrissey, D. T. Bolvin, S. Curtis, R. Joyce, B. McGavock, and J. Susskind, 2001: Global precipitation at one-degree daily resolution from multisatellite observations. *J. Hydrometeorol.*, **2**, 36–50.
- Jones, C., D. E. Waliser, and C. Gautier, 1998: The influence of the Madden–Julian oscillation on ocean surface heat fluxes and sea surface temperature. *J. Climate*, **11**, 1057–1072.
- Kalnay, E., and Coauthors, 1996: The NCEP/NCAR 40-Year Reanalysis Project. *Bull. Amer. Meteor. Soc.*, **77**, 437–471.
- Kang, I.-S., and Coauthors, 2002: Intercomparison of atmospheric GCM simulated anomalies associated with the 1997/98 El Niño. *J. Climate*, **15**, 2791–2805.
- Krishnamurti, T. N., D. K. Oosterhof, and A. W. Mehta, 1988: Air–sea interaction on the timescale of 30 to 50 days. *J. Atmos. Sci.*, **45**, 1304–1322.
- Lau, K.-M., and C.-H. Sui, 1997: Mechanisms of short-term sea surface temperature regulation: Observations during TOGA COARE. *J. Climate*, **10**, 465–472.
- Madden, R. A., and P. R. Julian, 1972: Description of global-scale circulation cells in the tropics with a 40–50 day period. *J. Atmos. Sci.*, **29**, 1109–1123.
- Oppenheim, A. V., and R. W. Schaffer, 1975: *Digital Signal Processing*. Prentice Hall, 585 pp.
- Pfeffer, R. L., J. Ahlquist, R. Kung, Y. Chang, and G. Li, 1990: A study of baroclinic wave behavior over bottom topography using complex principal component analysis of experimental data. *J. Atmos. Sci.*, **47**, 67–81.
- Reynolds, W. R., and T. M. Smith, 1994: Improved global sea surface temperature analyses using optimum interpolation. *J. Climate*, **7**, 929–948.
- Rowell, D. P., C. Folland, K. Maskell, and N. Ward, 1995: Variability of summer rainfall over tropical North Africa (1906–92): Observations and modeling. *Quart. J. Roy. Meteor. Soc.*, **121**, 669–704.
- Schubert, S. D., and M. L. Wu, 2001: Predictability of the 1997 and 1998 South Asian summer monsoon low-level winds. *J. Climate*, **14**, 3173–3191.
- Shinoda, T., H. H. Hendon, and J. Glick, 1998: Intraseasonal variability of surface fluxes and sea surface temperature in the tropical western Pacific and Indian Oceans. *J. Climate*, **11**, 1685–1702.
- , —, and —, 1999: Intraseasonal surface fluxes in the tropical western Pacific and Indian Oceans from NCEP reanalyses. *Mon. Wea. Rev.*, **127**, 678–693.
- Slingo, J. M., and Coauthors, 1996: Intraseasonal oscillations in 15 atmospheric general circulation models: Results from an AMIP diagnostic subproject. *Climate Dyn.*, **12**, 325–357.
- Sperber, K. R., J. M. Slingo, P. M. Innes, and W. K.-M. Lau, 1997: On the maintenance and initiation of the intraseasonal oscillation in the NCEP/NCAR reanalysis and in the GLA and UKMO AMIP simulations. *Climate Dyn.*, **13**, 769–795.
- Waliser, D., K.-M. Lau, and J. H. Kim, 1999: The influence of coupled sea surface temperatures on the Madden–Julian oscillation: A model perturbation experiment. *J. Atmos. Sci.*, **56**, 333–358.
- Wang, B., and X. Xie, 1998: Coupled modes of the warm pool climate system. Part I: The role of air–sea interaction in Madden–Julian oscillation. *J. Climate*, **11**, 2116–2135.
- Weickmann, K. M., G. R. Lussky, and J. E. Kutzbach, 1985: Intraseasonal (30–60 day) fluctuations of outgoing longwave radiation and the 250-mb streamfunction during northern winter. *Mon. Wea. Rev.*, **113**, 941–961.
- Wu, M.-L., S. Schubert, and N. E. Huang, 1999: The development of the South Asian summer monsoon and the intraseasonal oscillation. *J. Climate*, **12**, 2054–2075.
- Xie, P., and P. A. Arkin, 1997: Global precipitation: A 17-year monthly analysis based on gauge observations, satellite estimates, and numerical model outputs. *Bull. Amer. Meteor. Soc.*, **78**, 2539–2558.
- Yasunari, T., 1981: Structure of an Indian summer monsoon system with a period around 40-days. *J. Meteor. Soc. Japan*, **59**, 336–354.
- Zhang, C., 1996: Atmospheric intraseasonal variability at the surface in the tropical western Pacific Ocean. *J. Atmos. Sci.*, **53**, 739–758.
- Zhang, G. J., and M. J. McPhaden, 1995: The relationship between sea surface temperature and latent heat flux in the equatorial Pacific. *J. Climate*, **8**, 589–605.